theRmalUAV: an R package to clean and correct thermal UAV data for accurate land surface temperatures

Christophe Metsu[a,*], Wouter H. Maes[b], Sam Ottoy[a,c,d], Koenraad Van Meerbeek[a,e]

[a] *Division Forest, Nature and Landscape, Department Earth and Environmental Sciences, KU Leuven, 3000 Leuven, Belgium*
[b] *UAV Research Centre, Department of Plants and Crops, Ghent University, 9000 Ghent, Belgium*
[c] *Bio-Research, PXL University College, 3590 Diepenbeek, Belgium*
[d] *Center for Environmental Sciences, Hasselt University, 3590 Diepenbeek, Belgium*
[e] *KU Leuven Plant Institute, KU Leuven, 3000 Leuven, Belgium*
[*] *Corresponding author. christophe.metsu@kuleuven.be*

Keywords: Drones, Remote Sensing, Thermal Infrared, TIR, UAS, Unmanned Aerial Systems, Unoccupied Aerial Vehicles

Abstract

Thermal cameras mounted on unoccupied aerial vehicles (UAVs) are increasingly utilized across various environmental research fields, including hydrological modelling, wildfire detection, urban heat island studies, microclimate and precision agriculture. However, several steps are needed to convert the measured thermal signal to more relevant land surface temperature (LST). Since a number of users may have limited expertise in thermal remote sensing or data processing, necessary thermal corrections are often neglected or not performed correctly in research, even though this can result in substantial discrepancies of up to 5 °C in extreme cases when absolute LST is required. We facilitate the processing by introducing a new R package, `theRmalUAV`, which offers two workflows: an orthomosaic-based and an image-based workflow. The orthomosaic workflow consists of a single function to apply on an orthomosaic, while the image-based workflow provides greater flexibility, accommodating intra-flight variations in atmospheric conditions. Key components of the package include correcting for atmospheric interactions, background temperature, spatial emissivity using NDVI and land cover, and the influence of changing weather conditions on LST. Additionally, we introduce a novel method for accounting for rapid changes in illumination during flights. The package also includes functions for data cleaning, co-registration, and reporting. The package currently supports 11 different thermal sensors, covering the vast majority of thermographic cameras used today. The importance of these corrections and the implementation of the package are demonstrated through two use cases involving TeAx and DJI thermal cameras, under both ideal and challenging conditions.

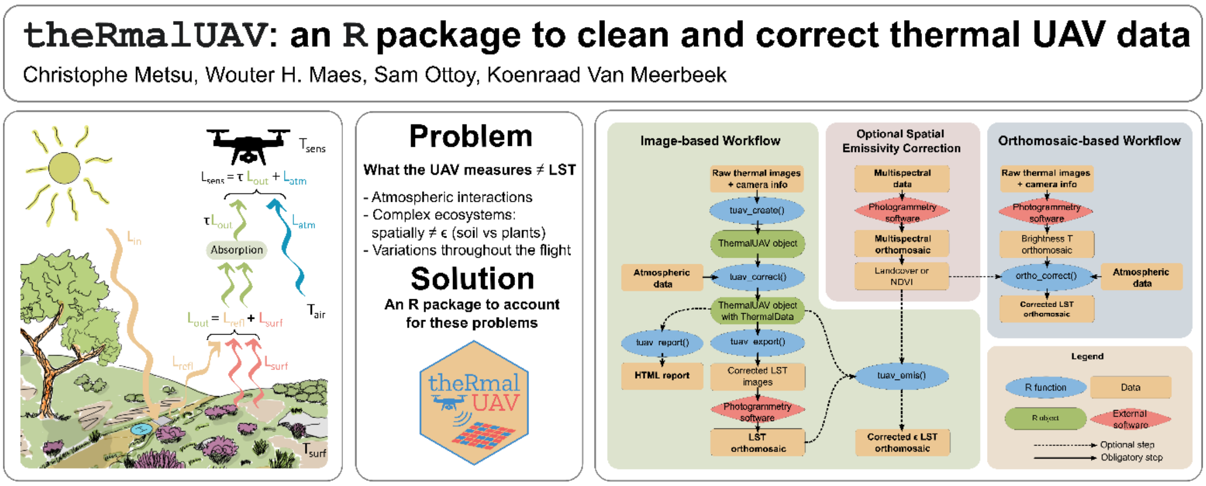

1. Introduction

Surface temperature is a critical variable across various domains, ranging from industrial applications to environmental studies. It serves as a key parameter in describing the energy balance between a surface and its surroundings, primarily due to its direct relationship with emitted long-wave infrared radiation (LWIR, 8-14 µm). This energy balance, or derived thermal metrics, can provide deeper insights into the properties and processes occurring within the corresponding object. Surface temperature has a broad spectrum of applications. In search and rescue missions, it is utilized to locate missing persons or track wildlife (Rudol and Doherty, 2008). In industrial contexts, it is employed for inspecting solar panels (Liao and Lu, 2021; Vlaminck et al., 2022), monitoring power lines (Dai et al., 2025), and identifying thermal leaks in buildings (Rakha et al., 2018).

Moreover, surface temperature is invaluable in environmental research and applications. Its potential is being explored in diverse fields, including hydrological modelling (Aicardi et al., 2017), coastal water quality estimation (Cheng et al., 2022), evaporation estimation (Hoffmann et al., 2016), urban heat island studies (Henn and Peduzzi, 2024; Wu et al., 2022), wildfire detection (Allison et al., 2016), and land use modelling (Muro et al., 2018). It is also used for wildlife population estimation (Beaver et al., 2020; Mirka et al., 2022), identification of microclimatic refugia (Hoffrén and García, 2023), and vegetation monitoring. In precision agriculture, surface temperature is directly applied in the crop water stress index to detect stress and diseases (Messina and Modica, 2020; Santesteban et al., 2017; Stutsel et al., 2021).

Advancements in remote sensing technologies have led to cost reductions and the miniaturization of sensors, thereby promoting the increased utilization of unoccupied aerial vehicles (UAVs or drones) in environmental research (Manfreda et al., 2018). Compared to traditional handheld thermal cameras or thermal satellite imagery, UAVs provide high spatial resolution and flexibility, enabling the acquisition of spatially continuous datasets with very high resolution. The integration of thermal infrared cameras on UAV platforms allows for the measurement of incoming LWIR and the direct derivation of land surface temperatures (LST).

In instances where precise absolute temperatures are required, the temperature data obtained from UAVs (or other remote sensing platforms) may not provide an immediately accurate product. The reliability of the data is significantly affected by variability in camera accuracy, surface properties, and atmospheric conditions, leading to a discrepancy between LST and the temperature measured at the sensor. Consequently, thermal infrared data acquired from UAVs often require essential corrections.

The complexity of the necessary corrections and the potential lack of thorough background in thermal remote sensing among environmental scientists and other UAV researchers, often result in incomplete or incorrect application of these corrections. Therefore, we have developed the user-friendly R package theRmalUAV for cleaning and correcting thermal UAV data. The aim of this package is to facilitate the implementation of fundamental corrections necessary to obtain optimal results from UAV thermal imagery. The methods and workflow are partially based on the recommendations of Maes, Huete and Steppe (2017), and Heinemann et al. (2020), with additional new functionalities. To help users understand the features offered in this package, we will first provide an overview of some basic principles of thermal remote sensing and the key concepts employed in the package. Subsequently, we will discuss the general workflow and capabilities of the package and showcase its application in two use cases with different sensors (Section 4 and 5).

2. Thermal remote sensing background

Typical thermal infrared (TIR, 8-14 µm) cameras used on UAV platforms are based on microbolometer sensor arrays. This type of sensor is a thermistor radiation detector, which relates the absorbed incoming TIR radiation energy to the temperature-dependent electrical resistance of the material. They do not require expensive cooling, in contrast to alternative high-resolution photonic IR sensors, making them more cost-effective (Posch et al., 2009; Wood et al., 1992). Uncooled TIR cameras, however, require extensive and complex calibration processes, which are usually already implemented by the manufacturer, adding to the cost of the camera (Budzier and Gerlach, 2015). Such calibration establishes a relationship between the electrical resistance of a pixel of the uncooled microbolometer sensor, expressed as grey values, and the corresponding blackbody temperature. The temperature data are then stored as digital numbers (DN), usually as integers in a 16 or 32-bit tiff file format. To convert these DN values into usable temperatures in Kelvin or degrees Celsius, a linear constant is applied. The resulting temperature is referred to as the at-sensor temperature.

For most applications, the at-sensor temperature is not yet the desired temperature. The incoming TIR radiation at the sensor includes multiple components, which can be described with the following radiative transfer model (Figure 1*;* Jones and Vaughan, 2010):

$$L_{sens} = \tau\left(L_{surf} + L_{refl}\right) + L_{atm} \tag{1}$$

L_x represents the radiance, i.e. the amount of radiation energy emitted, reflected, transmitted, or received by a given surface, per unit solid angle, per unit projected area, per unit time (W m^{-2} sr^{-1}), of the corresponding TIR radiation of property "x”. In the radiative transfer model, L_{sens} stands for the radiance reaching the sensor, L_{surf} the radiance from the TIR radiation emitted by the surface, L_{refl} describes the fraction of downwelling TIR radiation reflected by the surface (1 - ϵ) and L_{atm} represents the upwelling TIR radiation emitted by the atmospheric layer between the surface and the camera. The radiation passing through the atmospheric layer is attenuated, which is accounted for by the atmospheric transmittance τ (value between 0 and 1). Furthermore, L_{sens} depends on both the wavelength and sensor-specific properties (e.g. the wavelength range to which the sensor is sensitive). Therefore, the TIR camera manufacturer considers a modified inverse Planck function when converting L_{sens} to the at-sensor temperature (T_{sens}), typically assuming transmittance and emissivity to be one (Heinemann et al., 2020).

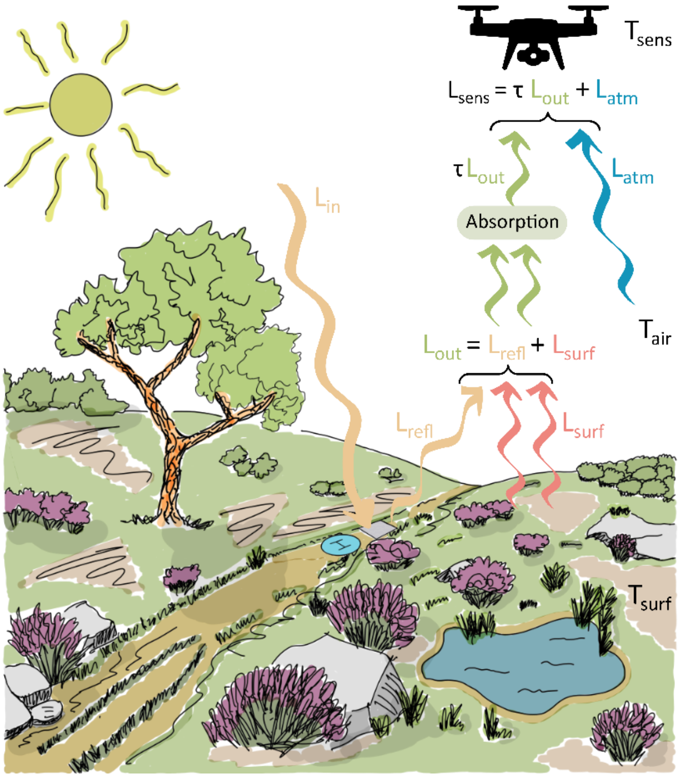

Figure 1. Visual representation of the TIR radiation components received by thermal sensor. L_{sens} denotes the radiance reaching the sensor (W m^{-2} sr^{-1}) and consists of (i) L_{atm}, representing the upwelling TIR radiation emitted by the atmospheric layer between the surface and the sensor, influenced by the free air temperature (T_{air}), (ii) L_{surf}, the radiance from the TIR radiation emitted by the surface, influenced by the surface temperature (T_{surf}), and (iii) L_{refl}, given by the fraction of downwelling/incoming TIR radiation (L_{in}) reflected by the surface. L_{refl} and L_{surf} are represented together as L_{out} and are both partially absorbed by the atmosphere, taken into account by the atmospheric transmittance τ. T_{sens} stands for the temperature perceived by the sensor (i.e., at-sensor temperature).

Natural objects are not perfect blackbodies, an idealized physical object that absorbs and emits all incident radiation. The degree to which an object absorbs and emits TIR radiation compared to a perfect black body at the same temperature is described by its emissivity (ϵ), ranging from 0 to 1. Consequently, the proportion of TIR radiation that is reflected is its complement:

$$L_{refl} = (1 - \epsilon)\, L_{in} \tag{2}$$

The relationship between radiant energy emitted by natural surfaces and their absolute temperature is described by the Stefan-Boltzmann law (Jones and Vaughan, 2010):

$$L_{surf} = \epsilon\, \sigma\, T_{surf}^4 \tag{3}$$

where L_{surf} represents the amount of radiation energy emitted by the surface, per unit projected area, per unit time (W m^{-2}), ϵ is the emissivity, σ is the Stefan-Boltzmann constant (5.67 10^{-8} W m^{-2} K^{-4}), and T_{surf} is the absolute temperature of the surface in Kelvin. Based on Eqs (1), (3) and as outlined in Maes, Huete and Steppe (2017) and Heinemann et al. (2020), the retrieval of LST can be formulated as follows:

$$LST = T_{surf} = \sqrt[4]{\frac{T_{sens}^4 - (1-\epsilon)\ \tau\ T_{bg}^4 - \frac{L_{atm}}{\sigma}}{\epsilon\ \tau}} \tag{4}$$

where T_{surf} is the desired LST of a surface with emissivity ϵ, T_{sens} the at-sensor temperature measured by the TIR camera, and T_{bg} the background temperature (to account for L_{refl}, see Section 2.2), all expressed in Kelvin. The emissivity (ϵ) and transmittance (τ) range between 0 and 1, and L_{atm} represents the upwelling TIR radiation emitted by the atmospheric layer between the surface and the sensor. L_{atm} can described using following equation:

$$L_{atm} = (1 - \tau)\, \sigma\, T_{air}^4 \tag{5}$$

with τ as the transmittance, and σ the Stefan-Boltzmann constant. T_{air} is the temperature of the atmospheric layer between the surface and the sensor (in Kelvin). As this is hard to quantify for the whole layer, the assumption is made that T_{air} is equal to the temperature at 1.5 - 2 meters height, and can therefore be measured by a weather station. According to Eq. (5), Eq. (4) becomes:

$$LST = T_{surf} = \sqrt[4]{\frac{T_{sens}^4 - (1-\epsilon)\ \tau\ T_{bg}^4 - (1-\tau)\, T_{air}^4}{\epsilon\ \tau}} \tag{6}$$

Following Eq. (6), the calculation of LST requires, next to the at-sensor temperature and surface specific emissivity, also some atmospheric properties, like transmittance, background temperature, and free air temperature. In the next sections we will go over the atmospheric correction, the concept of background temperature and emissivity correction.

2.1. Atmospheric correction

The atmospheric conditions during a thermal UAV flight exert a substantial influence on the TIR radiation received by the sensor, e.g. due to water vapor absorption, and thus the measured at-sensor temperature. Flying during humid, overcast conditions compared to a dry, sky clear day may result in different outputs for the same T_{surf}. After performing atmospheric correction to account for these conditions, the resulting temperature data is commonly referred to as brightness temperature:

$$T_{brightness} = \sqrt[4]{\frac{T_{sens}^4 - (1-\tau)\, T_{air}^4}{\tau}} \tag{7}$$

The transmittance of the atmosphere quantifies the proportion of L_{out} that can actually reach the thermal camera (Figure 1). It can be calculated using Eqs. (8),(9), by implementing parameters, like free air temperature (T_{air} (K), i.e. the temperature of the atmospheric layer between the surface and the sensor) and relative humidity ($\omega\%$, i.e. the amount of water vapor in the air compared to the maximum amount the air can hold at a given temperature), which can be retrieved from in situ measurements or nearby weather stations. First, the water vapor content (ω, in mm) is calculated based on relative humidity and air temperature:

$$\omega = \omega\%\ exp\left(h_1\, T_{air}^3 + h_2\, T_{air}^2 + h_3\, T_{air} + h_4\right) \tag{8}$$

where $\omega\%$ is the relative humidity ranging from 0 to 1, and T_{air} is the free air temperature (°C). In addition, h_1, h_2, h_3, and h_4 are specific parameters defined for the temperature window from -40 to 120 °C, where $h_1 = 6.8455 \times 10^{-7}$, $h_2 = -2.7816 \times 10^{-4}$, $h_3 = 6.939 \times 10^{-2}$, and $h_4 = 1.5587$ (Minkina and Klecha, 2015; Tran et al., 2017). Subsequently, transmittance (τ) can be computed using the water vapor content and the distance between the sensor and the measured object (d, in m):

$$\tau = K_{atm}\, exp\left[-\sqrt{d}\left(\alpha_1 + \beta_1\sqrt{\omega}\right)\right] + (1 - K_{atm})\, exp\left[-\sqrt{d}\left(\alpha_2 + \beta_2\sqrt{\omega}\right)\right] \tag{9}$$

with K_{atm} a specific scaling factor of atmospheric damping, representing the combined effect of absorption by gaseous components and the atmospheric turbidity ($K_{atm} = 1.9$), together with the atmospheric attenuation without water vapor ($\alpha_1 = 0.0066$, $\alpha_2 = 0.0126$), and the attenuation of water vapor ($\beta_1 = -0.0023$, $\beta_2 = -0.0067$) (Minkina and Klecha, 2015; Tran et al., 2017). The distance between the sensor and the measured object is a measure of the amount of atmosphere which interferes with the radiation.

2.2. Background temperature and emissivity correction

To account for the atmospheric conditions above the UAV, and therefore the reflected downwelling TIR radiation (L_{refl}, Figure 1), the concept of background temperature (T_{bg}) can be used, representing the "temperature of the sky". This can be easily determined by retrieving the corresponding brightness temperature of a panel covered with (crumpled) aluminium foil using the TIR camera (Maes, Huete and Steppe, 2017; Heinemann et al., 2020). Due to its emissivity of typically less than 0.03, aluminium foil reflects almost all TIR radiation (Frolec et al., 2019). The sensor thus measures all TIR radiation emitted by the sky.

When T_{bg} is not measured, it can be estimated using the air temperature (Maes and Steppe, 2012):

$$T_{bg} = \sqrt[4]{\epsilon_{clr}\, F\, T_{air}^4} \tag{10}$$

with T_{bg} the background temperature, ϵ_{clr} the sky emissivity at clear sky, T_{air} the air temperature in Kelvin, and F a measure of the cloudiness of the sky (where F ≥ 1). A commonly used value for ϵ_{clr} is 0.7 (Sedlar and Hock, 2009). Under clear sky conditions, F equals 1, thus a T_{air} value of 20 °C (293.15 K) corresponds to a T_{bg} of -5 °C (268.15 K). In overcast conditions, F approximates 1.4, bringing T_{bg} in line with T_{air}.

Following from Eq. (3), (4), emissivity is a crucial parameter for relating surface temperature to the measured LWIR, describing the extent to which the surface deviates from a black body. Emissivity has the largest impact of all parameters in Eq. (6) on obtaining accurate LST (Maes and Steppe, 2012); an error of 1% in emissivity corresponds to a temperature difference of 0.75K (Jones et al., 2003) in sunny conditions. This influence becomes even more significant in sunny conditions and with lower emissivity values (see the example in Section 4). However, obtaining the correct emissivity value is very challenging and usually two major assumptions are being made. First, emissivity is assumed to be constant in the spectral range of 8-14 µm, although it is wavelength-dependent, varying slightly across this range (Salisbury and D'Aria, 1992). Second, angular effects are ignored to simplify the retrieval methods, even though emissivity varies with the viewing angle (Cuenca and Sobrino, 2004). Emissivity is often estimated using indirect methods, such as lookup tables, empirical relationships with other metrics, or by solving radiometric equations (Li and Becker, 1993; Van de Griend and Owe, 1993). It should be noted that the emissivity of individual objects, such as leaves, can be measured. However, the emissivity of vegetation as a whole differs from that of individual vegetation components and is generally higher due to the shadow cavities within the vegetation, which resemble black boxes. Thus, emissivity at the vegetation level cannot be directly measured (Maes and Steppe, 2012).

While using one fixed value might be ok for a homogenous surface, this approach is too simplistic in more complex ecosystems. The implementation of vegetation indices, such as the NDVI (the normalized difference vegetation index), enable spatially explicit estimation of thermal emissivity by applying an empirical relationship between the index and thermal emissivity (Kerr et al., 2004). The NDVI is given by:

$$NDVI = \frac{NIR-R}{NIR+R} \tag{11}$$

with NIR and R the reflectance of near-infrared and red radiation respectively and lies between -1 to 1. It can be useful to differentiate between vegetation densities, as well as land cover types by setting simple thresholds. Valor and Caselles (1996) proposed a method where emissivity is given as a function of vegetation and bare soil emissivity values with vegetation cover fraction as weight:

$$\epsilon = \epsilon_{veg} \ P_v + \epsilon_{soil} \ (1 - P_v \ ) + d\epsilon \tag{12}$$

where P_v is the vegetation cover fraction, ϵ_{veg} is the vegetation emissivity, ϵ_{soil} the bare soil emissivity, and $d\epsilon$ a term due to cavity effect (surface roughness). This term can be written as $d\epsilon = 4 \, \langle d\epsilon \rangle \, P_v \, (1 - P_v)$, where $\langle d\epsilon \rangle$ is a simplified parameter ($\langle d\epsilon \rangle \approx 0.01$). The vegetation cover fraction can simply be determined by (Carlson and Ripley, 1997; Sobrino et al., 2008):

$$P_v = \left(\frac{NDVI - NDVI_{soil}}{NDVI_{veg} - NDVI_{soil}} \right)^2 \tag{13}$$

with $NDVI_{veg}$ and $NDVI_{soil}$ the NDVI of respectively full vegetation and bare soil. This way of prediction the emissivity is used in the NDVI threshold method (Sobrino and Raissouni, 2000). By setting two well-chosen NDVI thresholds, the landscape can be divided into three classes: bare soil, vegetation, and mixed pixels, where the latter relies on Eq. (12) to estimate the emissivity. The NDVI threshold method is often used because of its simplicity and already successfully applied to various sensors (Li et al., 2013), such as AVHRR (Sobrino and Raissouni, 2000) and MODIS (Sobrino et al., 2003). Moreover, the need for accurate atmospheric corrections when calculating P_v is not necessary because of the use of a normalized vegetation index (Li et al., 2013). A downside is the assumption that the surface only consists of soil and vegetation (e.g., water is not taken into the equation) (Tang et al., 2015). Furthermore, a priori knowledge on ϵ_{veg}, ϵ_{soil}, $NDVI_{veg}$, and $NDVI_{soil}$ is needed. The method is not limited to soil and vegetation and can for example be used to create an emissivity gradient between healthy, green and dead or senescent vegetation using emissivity values as described in Salisbury and D'Aria (1992).

The classification-based emissivity method is another approach to account for the spatial variation in emissivity. In essence, a land cover classification is performed and the corresponding emissivity values are assigned to each class (Li et al., 2013). This method heavily relies on the accuracy of the classification and possible limitations in number of classes. Furthermore, relevant emissivity values are available in databases like Salisbury and D'Aria (1992). In general, dense vegetation has a high emissivity value between 0.98 and 0.99 (Rubio et al., 1997). However, it is also related to the state of the vegetation and can, for example, substantially decrease for dry vegetation (Lillesand et al., 2015).

3. The `thermalUAV` workflow and functionalities

The R package can be installed from [christophemetsu/theRmalUAV: An R package to clean and correct thermal UAV data]. The functionalities of the theRmalUAV package are grouped into two workflows (Figure 2):

1. **Image-based workflow:** streamlines individually correcting thermal images before combining them into an orthomosaic using external photogrammetry software. This approach allows for adjustments to temperature and relative humidity variations over prolonged flight durations.

2. **Orthomosaic-based workflow:** performs the corrections directly on an already stitched brightness temperature orthomosaic. The workflow is intended for scenarios where processing of the individual raw thermal images is either unnecessary or unfeasible (e.g., due to a lack of weather station data). In this context, intra-flight atmospheric variability is not considered. However, this workflow is particularly beneficial for multispectral cameras where the thermal band has a low resolution and relies on other bands for stitching in photogrammetry software (e.g. Micasense Altum).

In both workflows, users have the option to include a spatially explicit emissivity correction if multispectral data or a land cover map is available, though this is optional, it is highly recommended. In the image-based workflow, the *tuav_emis()* post-processing function is used to correct a LST orthomosaic created following the image-based workflow. In the orthomosaic-based workflow, on the other hand, the spatially explicit emissivity correction is directly embedded in the ortho_correct() function.

Figure 2 provides an overview of the core functions of both workflows and their most important steps are discussed below. More advanced functionalities and options are discussed in Section 3.2.5, 3.2.6 and 3.4. Additional information is available in the vignettes of the R package and on the website.

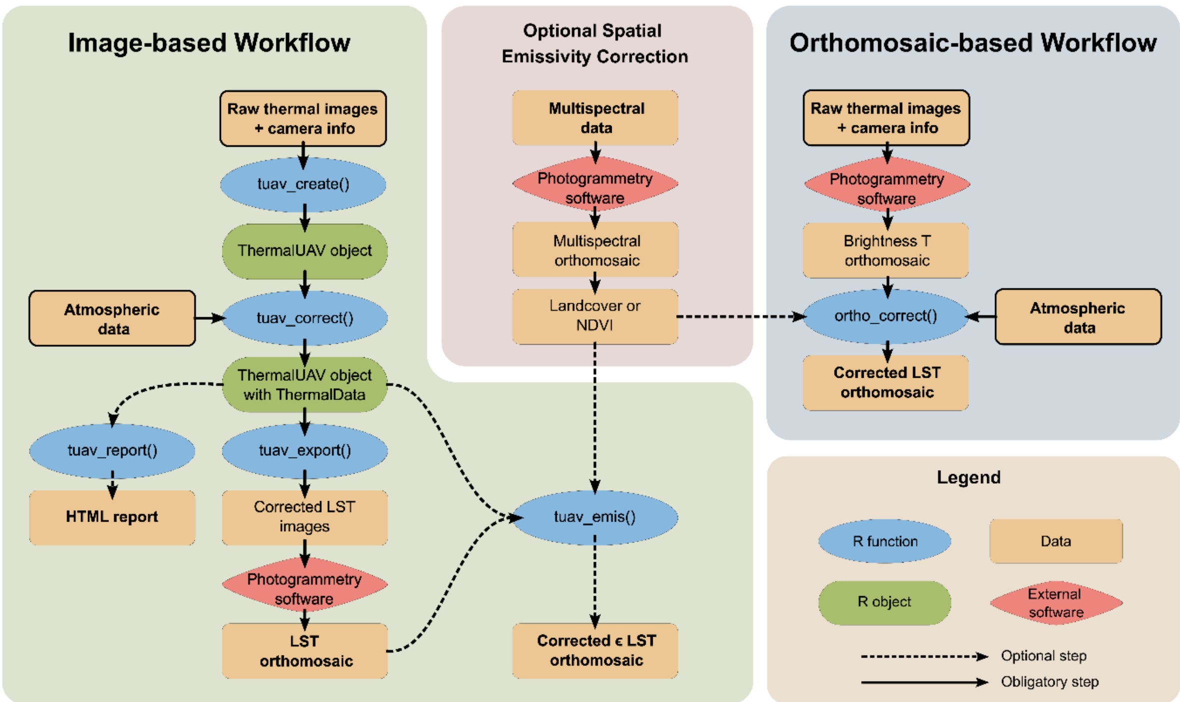

Figure 2. Overview of the theRmalUAV workflows. The green box presents the image-based workflow where raw thermal images are converted in corrected LST images. The othomosaic-based workflow is presented in the blue box, converting a brightness temperature orthomosaic to a corrected LST orthomosaic. The optional spatial emissivity correction starts in the pink box and can be implemented in both workflows. Initial data and end products are indicated in bold, the required inputs are outlined in black.

3.1. Data Collection

The initial step involves collecting the thermal images. To check if your TIR camera is compatible with the workflow, execute the function *tuav_cameras()* to view a list of supported cameras. Currently the package supports the following cameras: TeAx ThermalCapture (2.0), Micasense Altum(-PT), DJI Mavic 3T, DJI Mavic 4T, DJI Matrice 3TD, DJI Zenmuse H20N, DJI Zenmuse H20T, DJI Zenmuse H30T, DJI Matrice 30T (both normal and super-resolution mode). Read carefully the camera's user manual before use. It is, furthermore, advisable to conduct flights under homogeneous atmospheric conditions to avoid rapid transitions between sunny and cloudy conditions. To monitor atmospheric changes during the flight, it is recommended to use a portable weather station capable of measuring air temperature and relative humidity at high frequency, e.g. in 5-second intervals (Kelly et al., 2019; Maes, 2025). In the absence of a portable weather station, data from the nearest weather station could be used. As previously mentioned in Section 2.1, the background temperature (*Tbg*) can be accurately measured by placing a reference panel covered with crumpled aluminium foil on the ground and obtaining the corresponding brightness temperature using the TIR camera. Make sure that the aluminium foil panel is large enough, so it is covered by at least 9 pixels, to avoid mixed pixels and obtain an accurate reading.

3.2. The image-based workflow

3.2.1. Create ThermalUAV object

The image-based workflow is structured around a custom R object of class ThermalUAV. A ThermalUAV object comprises lists with slots for essential variables that will be filled and used along the way, facilitating a streamlined and flexible workflow. The variables are categorized into the following sections: Info, Position, Sharpness, Atmosphere, Smooth and ThermalData, where the latter stores the temperature data as a list of matrices (LST or brightness temperature, depending on the step and used parameters). The function *tuav_create()* creates a ThermalUAV object relying on the pathname to the thermal image folder, the camera name (check *tuav_cameras()*), the flight height, and optionally the path to an additional metadata data frame.

3.2.2. Conversion of at-sensor temperature to LST

The function *tuav_correct()* performs the necessary corrections at the image level on a ThermalUAV object, given the required atmospheric data. The atmospheric data can be provided in one of the following formats: (i) a single measurement of air temperature (T_{air}) and relative humidity ($\omega\%$), (ii) T_{air} and/or $\omega\%$ as vectors with lengths corresponding to the number of images in the ThermalUAV object, (iii) a data frame containing T_{air} and $\omega\%$ along with datetime information covering at least the whole duration of the flight, or (iv) in the absence of measured air temperature, T_{air} can also be estimated using a trimmed mean from the pixel values in the thermal image. For each image, the water vapor content and the transmittance is calculated using respectively Eqs. (8), (9), followed by the calculation of the LST using a single emissivity value, provided by the user (Eq. (4)). In occasions where background temperature (T_{bg}) was not measured, T_{bg} will be estimated following Eq. (10). The user should then specify if the conditions were sky clear or overcast. The function reads the TIFF files and stores the LST values as a list of matrices under ThermalData. Eventually an updated ThermalUAV object is returned including the LST information. Note: if emissivity is set to 1, this function does not correct for background temperature and emissivity (Eq. (4)). In that case, the returned temperature data will be the brightness temperature. This is recommended if emissivity is corrected spatially afterwards (see Section 3.2.4). Furthermore, *tuav_correct()* does not account for the effect of T_{air} on LST (Maes, Huete and Steppe, 2017), but can be corrected using the post-processing function *tuav_smooth()* (see section 3.2.6).

3.2.3. Exporting and mosaicking

Once all the desired corrections have been applied, the ThermalData can be exported as geotagged TIFF files using function *tuav_export()*. To efficiently store the temperature data with a two-decimal precision, each image is written as centikelvin in a 16 bit TIFF file labelled "original_filename_corrected.tif". These files include the necessary metadata for further processing, including GNSS position and altitude, pitch, roll yaw, and more. After saving all the corrected thermal images, you can align and mosaic them using commercial photogrammetry software, such as Agisoft Metashape or Pix4D Mapper, to create a land surface temperature orthomosaic. Since the data is stored in centikelvin, it should be divided by 100 and then subtracted by 273.15 to convert the resulting temperatures to degrees Celsius. If desired an HTML-report can be created using *tuav_report()*. This report provides an overview of the executed corrections with their corresponding parameters, camera locations in an interactive map, and general background information about the mission.

3.2.4. Emissivity correction

When your area of interest comprises multiple land cover types and/or a heterogeneous landscape, spatially explicit emissivity correction is recommended. As described in Section 3.2.2, the *tuav_correct()* function uses only one emissivity value, as spatially explicit emissivity correction is not accurate at the image level due to uncertainties in image positioning and viewing angles. The post-processing function *tuav_emis()* does allow for emissivity correction on georeferenced LST orthomosaics. To apply the emissivity correction, the pixel values are first backtransformed to at-sensor temperature, given the original parameters provided in the corresponding ThermalUAV object. The land surface temperature on pixel level is now calculated with a spatially explicit emissivity value using one of the following methods: (i) the NDVI threshold method (as described in 2.2), given the

NDVI map and providing the necessary thresholds directly in the function; (ii) the land cover map with a two-column matrix containing the values of the land cover classes in the first column and their corresponding emissivity values in the second; or (iii) directly using an emissivity map. The LST orthomosaic and the map to be used for the correction can be provided as either a *terra::SpatRaster* object or as pathname to the map stored locally on your personal computer.

3.2.5. Accounting for varying weather conditions

Conducting thermal flight missions under stable, sunny conditions is recommended due to the challenges associated with correcting illumination changes in thermal data (Maes, 2025). Rapid changes in illumination can lead to heterogeneity and distortion in the final land surface temperature orthomosaic. While techniques such as radiometric block adjustment are employed to address this issue in multispectral UAV imagery, they remain under-investigated for thermal UAV data (Wang et al., 2024). Maes, Huete and Steppe (2017) proposed a technique to account for the effect of varying air temperature on LST using a high temporal resolution air temperature dataset:

$$T_{surf_{correct}} = T_{surf} - T_{air} + T_{air_{mean}} \tag{14}$$

where $T_{surf\_corrected}$ is the corrected surface temperature (T_{surf}), T_{air} is the air temperature at the moment of image capture, and T_{air_mean} is the mean air temperature during the flight. This correction method is incorporated in the package under the function *tuav_smooth()*, with the parameter *method* set to *"T_air"*. A limitation of this technique is its inability to capture spatially explicit changes in illumination and local wind gusts, as typically only one portable weather station is placed at a fixed location. Additionally, obtaining such a dataset is not always feasible.

To address these limitations, we propose a similar technique based on the temperature of the thermal images themselves. First, the trimmed mean (with a fraction of 20%) of each image in the ThermalData is calculated to avoid the influence of extreme temperatures (Eq. (15)). Second, the smoothed temperature (T_{smooth}) is calculated as the mean of a moving window with a length equal to *smoothlength* (Eq. (16)). Finally, the image is corrected by subtracting its corresponding T_{smooth} and adding the mean of T_{smooth} (Eq. (17)).

$$T_{image,mean}[i] = mean\big(T_{image}[i], 0.2\big) \tag{15}$$

$$T_{smooth}[i] = mean\left(T_{image,mean}\left[i - \frac{smoothlength}{2} : i + \frac{smoothlength}{2}\right]\right) \tag{16}$$

$$T_{image_{corrected}} = T_{image} - T_{smooth} + T_{smooth_{mean}} \tag{17}$$

The newly proposed method is also embedded in the function *tuav_smooth()*. To perform the correction using this method, the parameter *method* should be set to *"image"*. This correction should always be performed after calling *tuav_correct()* as it relies on the temperature data stored under

ThermalData in the ThermalUAV object. The performance of this correction will be discussed using a use case in Section 5.

3.2.6. Other functionalities

The R package offers additional functionalities beyond those previously described. Note, to keep a clear overview, only the basic functions are represented in Figure 2. We will briefly outline some functions in Table 1, but more functions and detailed information are available in the package's reference and vignettes. All the functions require a ThermalUAV object as input and, except *tuav_view()*, return an updated ThermalUAV object.

Table 1: an overview of additional functionalities within the image-based workflow. These functions can only be applied on ThermalUAV objects at any time during the processing unless stated otherwise.

	Function	Description
Position functions	*tuav_loc()*	Calculates the camera locations/image extents as *terra::SpatVector* object. Optionally the mean frontal overlap can be calculated.
	tuav_view()	Plots the camera locations/image extents in an interactive map. This allows for visual checks aiding in intermediate cleaning steps.
	tuav_coreg()	Optimizes thermal camera locations and viewing angles using co-registered high-resolution cameras with a high precision GNSS system. Can be done directly or by using the optimized camera locations after stitching the high-resolution camera in Agisoft Metashape. In the latter case *coreg_prep()* is needed to set the data in the right format. Optimized cameras are stored in an updated ThermalUAV object and are used when exporting.
Cleaning	*tuav_persec()*	Reduces the data volume by specifying the number of images to retain per second, keeping the ones with the highest sharpness. Can be useful for thermal cameras recording at a fixed high frequency rate.
	tuav_reduc()	Reduces the data volume either based on a minimal frontal overlap or minimal sharpness quality. Can be useful for thermal cameras recording at a fixed high frequency rate.

3.3. The orthomosaic-based workflow

The orthomosaic-based workflow corrects brightness temperature orthomosaics. This means that the raw thermal images are first stitched in a photogrammetry software. Possibly, a conversion to Kelvin might be required as some cameras provide their data as centikelvin or as DN where a linear constant should be applied. The *ortho_correct()* function relies on one value for T_{air} and $\omega\%$, as intra-flight atmospheric variability is not considered. The emissivity value can be set to a single value for the entire map, or you have the option to spatially account for it in a similar way as described in Section 3.2.4.

3.4. DJI Thermal IR Processing

Thermal images captured with a DJI (Da-Jiang Innovations) camera are stored in a specific way and require preprocessing before getting to actual temperature information. Therefore, the DJI Thermal IR Processing (DIRP) functionality, as used in the DJI thermal Analysis Tool, is also incorporated into the

R package through the function *tuav_dji()*. The function is not part of the image-based workflow as it does not return a ThermalUAV object, however, it does require a ThermalUAV object as input to work with the metadata. The function, furthermore, depends on object distance, relative humidity, emissivity and reflected temperature to convert the data to LST. Please note should be made that the underlying conversion is not made publicly available by DJI. When using the image-based workflow for DJI cameras, this function is embedded in *tuav_correct()*, meaning no additional preprocessing is required. In this case, the object distance is set to 1 and emissivity to 1 to achieve the at-sensor temperature, on which the regular processing is performed as outlined in Section 2. There are two prerequisites for using the R package for DJI cameras: (i) a version of Python must be installed on your system, subsequently, a virtual environment should be initialized using the function *dji_init()*, and (ii) it is only compatible with Windows and Linux systems, as the Dynamic Link Libraries provided by DJI are available only for these two systems.

4. Case 1: An empirical example of the Image-Based Workflow using ThermalCapture 2.0

4.1. Data collection

In this section, we present an example of the image-based workflow. The study area is a heterogenous patch within the Kalmthoutse Heide (Figure 3A), a heathland ecosystem in Belgium. The landscape consists of heather shrubs (*Calluna vulgaris*) on a sandy soil, interspersed with patches of moss and bare soil, some trees (*Pinus sylvestris*), and shallow ponds (Figure 3B). A short flight was conducted on July 19, 2024, at 14:00 local time under clear sky conditions. We used the DJI Matrice 300 RTK equipped with (i) the Micasense Altum-PT to collect multispectral information, and (ii) the TeAx ThermalCapture 2.0 with the ThermalCapture Calibrator to obtain thermal information. A single grid flight mission was performed at 75 m above ground level with a side overlap of 80% and flight speed of 4.5 m/s, resulting in a ground sampling distance of 3.28 cm for the multispectral data and 9.66 cm for the thermal images. During the flight, free air temperature and relative humidity were measured at 5-second intervals with a Kestrel 5500L environmental meter placed on a tripod of 1.5 m height. Mean air temperature and relative humidity during the flight were 28.3 °C and 42.7 %, respectively.

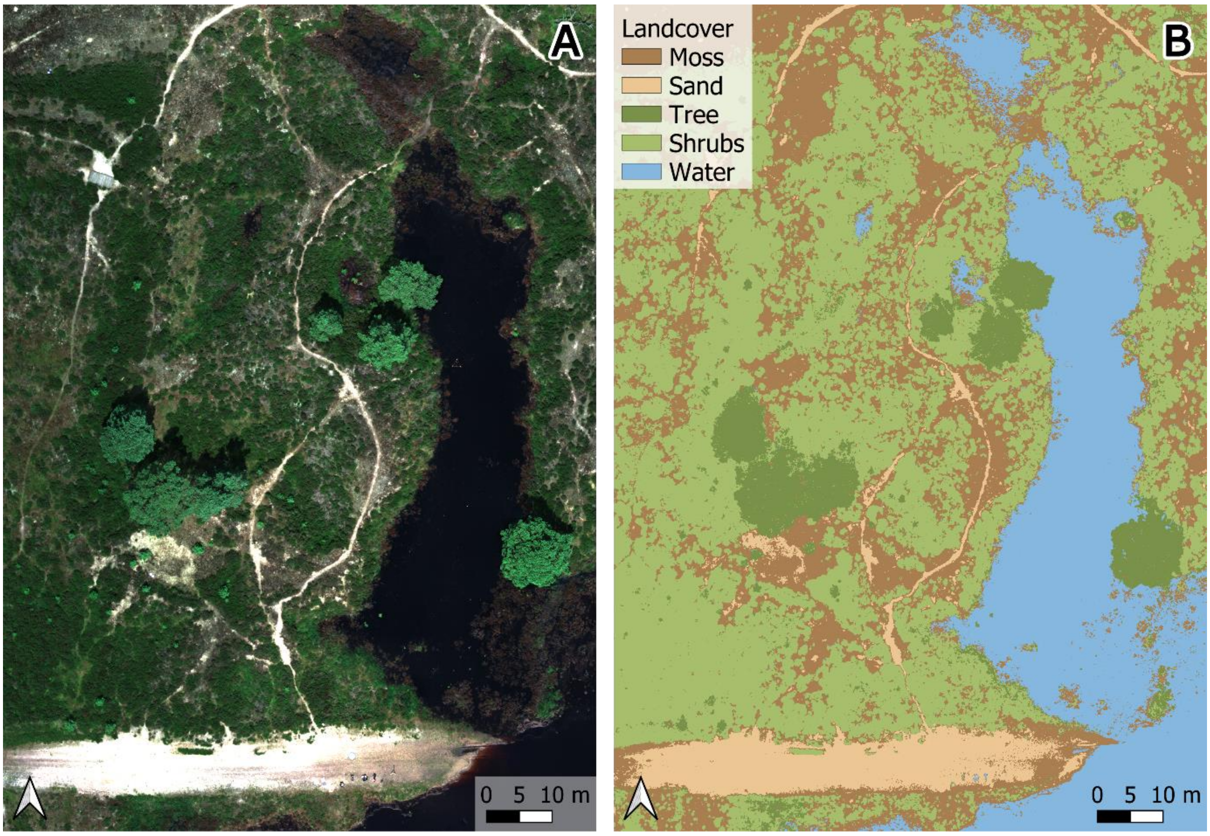

Figure 3. (A) RGB composite from the Micasense Altum-PT. (B) Land cover map showing the diverse landscape consisting of moss, sand, trees, shrubs and water.

4.2. Pre-processing

The multispectral imagery was processed using Agisoft Metashape Professional 2.0.0, following the recommended workflow (Agisoft Metashape, 2024). Reflectance calibration was performed using images of a 60 cm x 60 cm panel with 50 % reflectance taken at the flight altitude. As our thermal camera is co-registered with the Micasense Altum-PT, we will also demonstrate the optional co-registration workflow. Consequently, the camera references were exported as CSV file, including the rotation and estimated values with a precision of 7 decimal numbers. The thermal data, stored as TMC file, were converted to TIFF files using the ThermoViewer 3.0.10 software from TeAx. Metadata were exported as a single CSV file for all images.

4.3. Processing using the theRmalUAV package

The first step in the image-based workflow is creating the ThermalUAV object. After loading the theRmalUAV package into the environment, *tuav_create()* will create the ThermalUAV object (Section 3.2.1), here named as thermaluav. More information can be found in the help pages of the package.

```
library(theRmalUAV)
thermaluav <- tuav_create(path = "Data/TIFs/", camera = "ThermalCapture", meta_csv =
                                    "Data/TIFs/Example_meta.csv", flight_height = 75)
```

The ThermalCapture 2.0 is a thermal camera that records images at a rate of 8.33 Hz, resulting in a dataset of 1,237 images. The function *tuav_reduc()* (Table 1) is used to downsize the dataset, retaining only the sharpest images while setting a minimal frontal overlap. In this case, we chose for a minimal frontal overlap of 85%, resulting in a dataset of 125 images. The resulting ThermalUAV object is saved as a new variable (thermaluav_reduc) to avoid overwriting the previous ThermalUAV object.

```
thermaluav_reduc <-  tuav_reduc(thermaluav, method = "Overlap", min_overlap = 0.85)
```

Corrections can now be performed using *tuav_correct()* (Section 3.2.2). As we will later perform the optional, though recommended, spatially explicit emissivity correction, emissivity is initially set to 1 to obtain the brightness temperature. The free air temperature and relative humidity were provided in the format of a data frame obtained from the Kestrel environmental meter, allowing for image-level corrections.

```
thermaluav_correct <- tuav_correct(thermaluav_reduc, flight_height = 75, T_air = Kestrel, rel_hum = Kestrel,
                                   T_bg = 274.2, emiss = 1)
```

To correct for the effect of air temperature on the surface temperature, we can use the function *tuav_smooth()* (Table 1).

```
thermaluav_smooth <- tuav_smooth(thermaluav_correct, method = "T_air")
```

In our camera setup, the ThermalCapture 2.0 is fixed to our Micasense Altum-PT, allowing us to co-register the thermal data and benefit from the RTK accuracy of the Altum-PT camera. First, the data must be converted into the correct format using *coreg_prep()*. This function relies on camera references of the Altum-PT, which were exported from Agisoft Metashape, as mentioned in Section 0. Subsequently, the co-registration is performed using *tuav_coreg()*. Here, the rig offset values are provided in millimetres and are measured to the green band of the Altum-PT (band 2, the band to which other bands are offset). More information can be found in the vignettes and the help pages of the package.

```
sfm_cameras <- coreg_prep(img_path = "Data/Micasense/000/", SfM_option = "Agisoft Metashape",
                          opt_camera_path = "Data/Micasense/ReferenceCameras_example.txt",
                          camera_name = "Altum-PT_MSP", label = "_2", timezone = "UTC")
thermaluav_coreg <- tuav_coreg(thermaluav_smooth, opt_cameras = sfm_cameras, rig_offset = c(-46,-103,-20,
                               0, 0, 0))
```

Finally, we can export the data stored in the final ThermalUAV object. In this case, the ThermalData contains brightness temperatures as we used an emissivity of 1, and the camera locations were optimized during the co-registration. The information can be exported as TIFF files using *tuav_export()*.

```
tuav_export(thermaluav_coreg)
```

The TIFF files were processed in Agisoft Metashape using default parameters (Align > Build Point Cloud > Build DEM > Build Orthomosaic). The obtained orthomosaic was converted to degrees Celsius and exported as a GeoTIFF. To achieve land surface temperatures, we need to account for emissivity. The spatially explicit emissivity correction in this example is performed using the land cover option in the function *tuav_emis()*. First, a matrix is made linking the land cover labels to their corresponding emissivity (Table 2; (Rubio et al., 1997).

Table 2. Land cover classes with their corresponding emissivity values.

Label	Land cover	Emissivity
1	Dry mosses	0.962
2	Sand	0.914
3	Tree	0.983
4	Shrubs	0.984
5	Water	0.991

The function also requires the original temperature GeoTIFF - here the brightness temperature built in Agisoft Metashape -, a map to base our corrections on - here the land cover map -, and the last ThermalUAV object related to this project.

```
matrix <- matrix(c(1,2,3,4,5,0.962,0.914,0.983,0.984,0.991), ncol = 2)
thermaluav_emis <- tuav_emis(thermal_orig = "Data/Example_Tbright.tif",
                             thermal_uav = thermaluav_coreg,
                             temp = "C",
                             corrmap = "Data/Example_LC.tif",
                             method = "LC",
                             write_Ts = TRUE,
                             filename_Ts = "Example_Tsurf.tif",
                             LC_emiss_matrix = matrix)
```

4.4. Results

The final LST map illustrates the wide range of temperatures in this heterogeneous landscape on a hot, sunny day (Figure 4A). The bare sandy areas reach temperatures up to 50 °C, while the dark, dry mosses exhibit extreme surface temperatures up to 60°C due to the absorption of shortwave solar radiation and a lack of evapotranspiration. The shallow, still pond had a surface temperature of approximately 31°C.

The at-sensor temperature substantially underestimates the LST, with temperature differences reaching up to 5°C in certain instances (Figure 4B). The largest discrepancies are observed in areas with extreme temperatures and land covers with low emissivity values (e.g., bare sand, Figure 3B). The waterbody and trees, which generally have lower temperatures and emissivity values nearing 1, show smaller discrepancies (around 0.5°C).

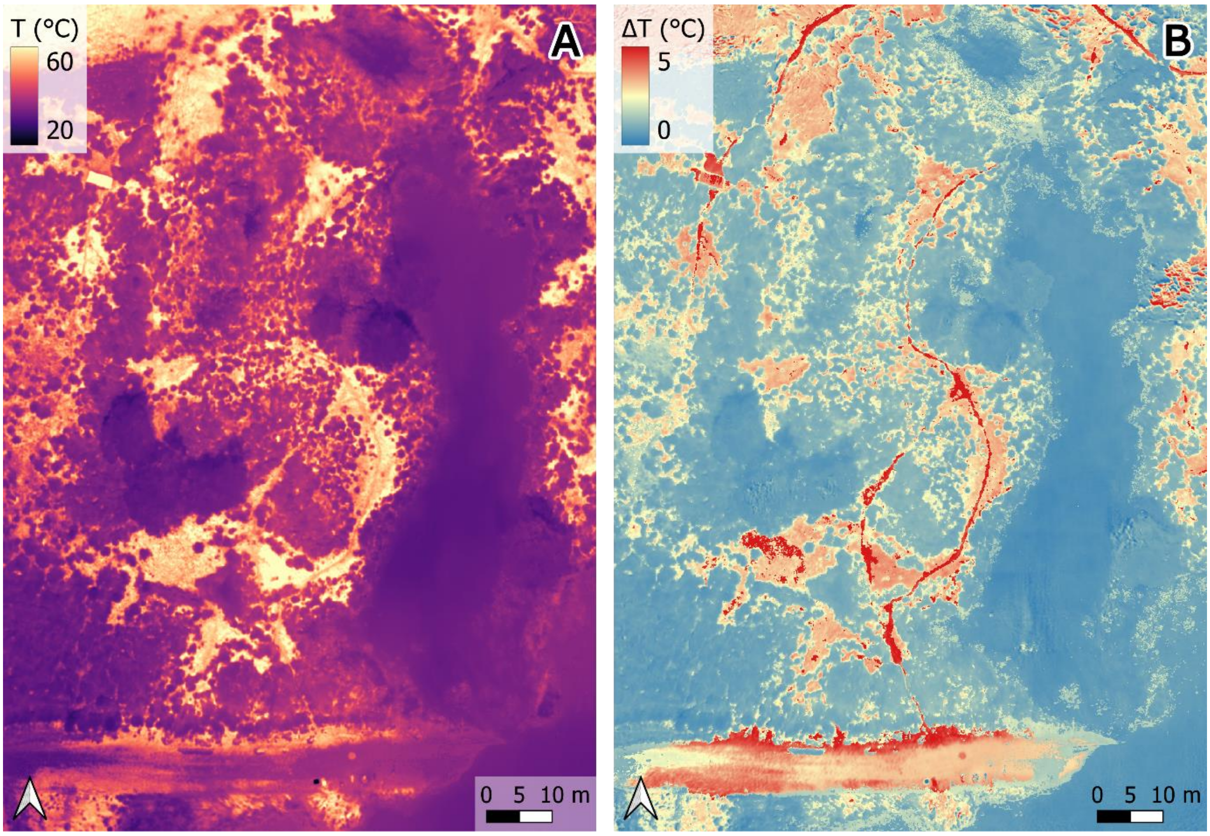

Figure 4. (A) Final LST map of the area representing the temperatures in degree Celsius. (B) Temperature difference (ΔT) between the LST and the at-sensor temperature.

To provide more insight into the effect of the corrections for this example, the differences between a range of at-sensor temperatures and the final LST per land cover class (and thus, emissivity), as well as the brightness temperature, are plotted in Figure 5. These differences were calculated using Eq. (6) with the mean atmospheric conditions during the flight: a transmittance of 0.9368, air temperature of 28.26 °C and a background temperature of 274.2 K. The emissivity values for each class are shown in Table 2, and to obtain the brightness temperature, the emissivity was set to 1. Note that the influence of the atmospheric correction is minimal when the at-sensor temperature approximates the free air temperature but becomes significant at very high temperatures (up to 2 °C in this example). When accounting for emissivity and background temperature, the discrepancies become more prominent, especially at extreme temperatures and where the surface substantially deviates from the black body behaviour. This trend aligns with Figure 4B, where the largest discrepancies occur on the bare soil (low emissivity) and at the patches of dry moss (extreme temperatures).

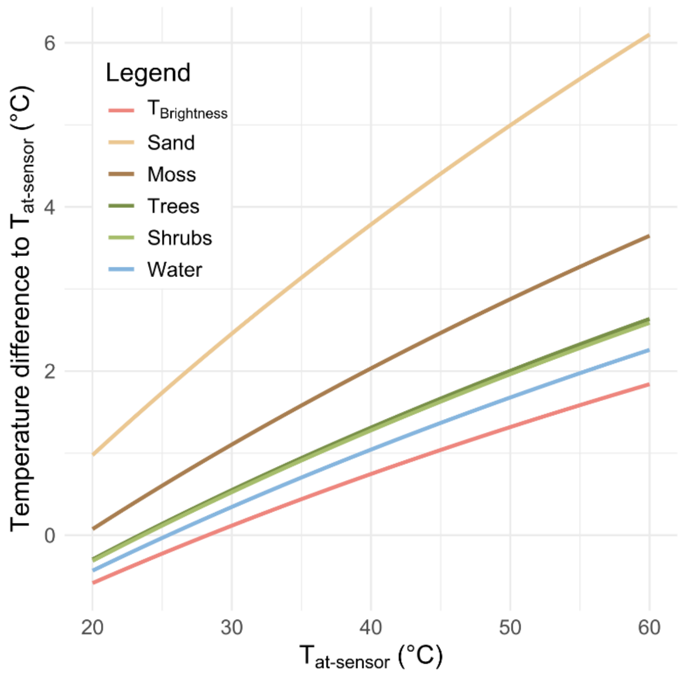

Figure 5: Temperature differences to the at-sensor temperature in sunny conditions for Case 1. With the brightness temperature ($\epsilon = 1$) in red becoming higher compared to at-sensor temperature when the at-sensor temperature exceeds the free air temperature. The differences to the final LST are given per land cover class as they each have a different emissivity ($\epsilon_{sand} = 0.914$, $\epsilon_{moss} = 0.962$, $\epsilon_{tree} = 0.983$, $\epsilon_{shrub} = 0.984$, $\epsilon_{water} = 0.991$). The differences are calculated using Eq. (6) with the mean atmospheric values during the flight: a transmittance of 0.9368, air temperature of 28.26 °C and a background temperature of 274.2 K.

5. Case 2: Accounting for variable weather conditions using the DJI Mavic 3T

5.1. Data Collection

In this second use case, we demonstrate the effect of the smoothing function *tuav_smooth()* on a flight conducted under variable weather conditions. The flight took place on September 13, 2024, at 12:25 local time over a potato field in Bottelare, Belgium. Initially, the flight conditions were sunny, but a cloud quickly covered the area, drastically altering the illumination (Figure 6A). The average air temperature was 16.1 °C, and the relative humidity was measured at 98 %. Thermal images were acquired using a DJI Mavic 3T at a flight altitude of 30 m. To generate the corresponding NDVI map (Figure 6D), we used the Micasense RedEdge Dual mounted on a DJI Matrice 350 RTK, earlier the same day under stable weather conditions. Eight ground control points (GCPs) were spread out across the field to align the thermal data with the NDVI map.

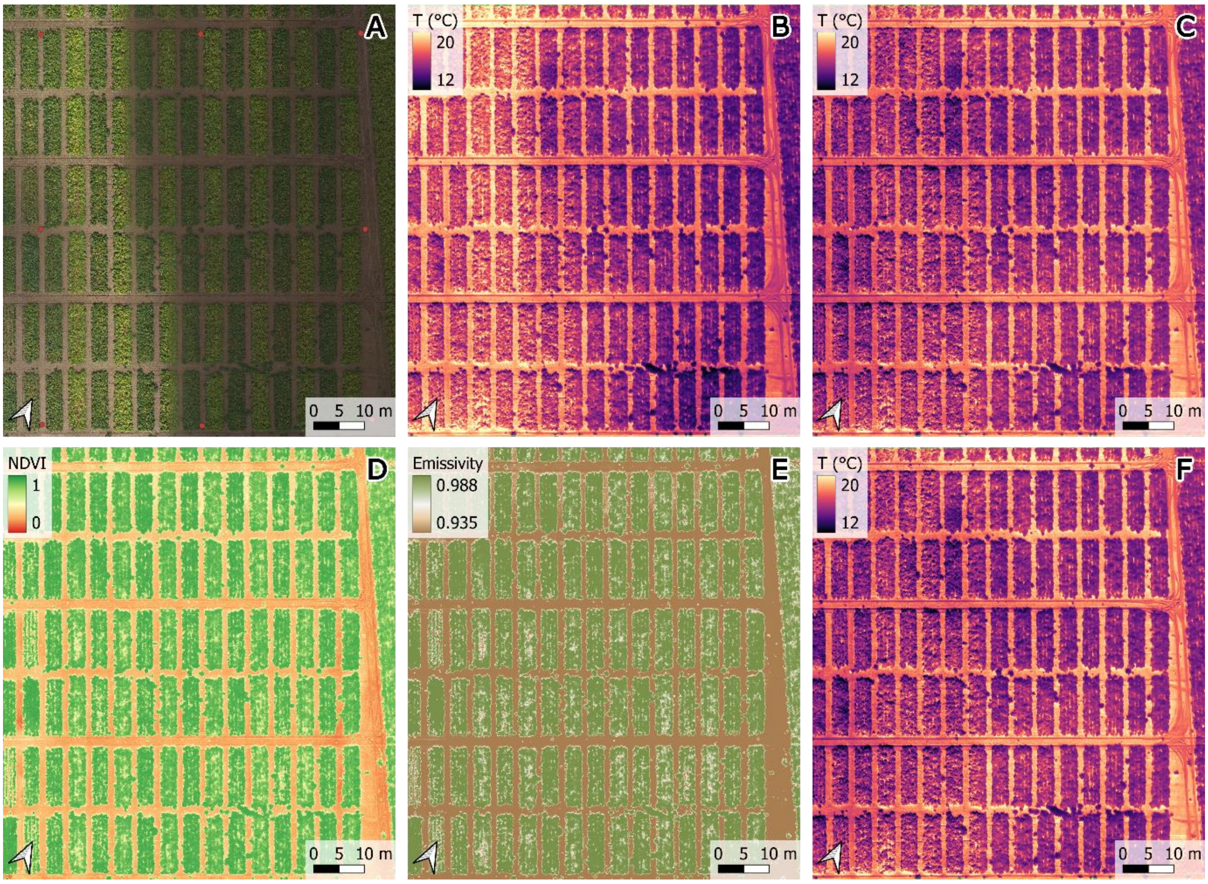

Figure 6. Potato field in Bottelare, Belgium. (A) RGB orthomosaic derived from the RGB camera on the DJI Mavic 3T, simultaneously captured with the thermal data, showing the fast change in illumination going from left to right. The red dots represent the locations of the ground control points. (B) Brightness temperature in °C before using the smoothing function, clearly showing the same pattern as the RGB data, influenced by the change in weather conditions. (C) Brightness temperature in °C after using the smoothing function, accounting for this change, resulting in a more homogenous output. (D) the corresponding NDVI map created from the Micasense RedEdge Dual, flown earlier that day under stable, sunny conditions. (E) Emissivity map of the field, the NDVI threshold method gives more nuances and a continuum of emissivity values between the thresholds. (F) Final LST in °C, where the warm bare soil, clearly defines the colder vegetation plots and the artefact of the varying weather conditions is accounted for.

5.2. The effect of *tuav_smooth()*

In this example, we used a DJI thermal camera. To work with the DJI cameras, the function *dji_init()* must first be called to set up the necessary configurations and access the Thermal SDK functionality embedded in the package (see Section 3.4). Similar to the empirical example in Section 4, we began by creating a ThermalUAV object using *tuav_create()*, specifying the path to the image folder and the camera name. Subsequently, the correction function was applied. In this case, we used a single value for air temperature (*T_air*) and relative humidity (*rel_hum*). Background temperature was not measured and thus was estimated using Eq. (10). As the majority of the flight was under overcast conditions, *SKC* was set to *FALSE*. Emissivity was set to 1, as spatial emissivity correction would be performed later, providing us with the brightness temperature. The data was then exported.

```
library(theRmalUAV)
dji_init()
path <- "H:/Thermal_Project/Data/M3T/”
```

```
thermaluav <- tuav_create(path = path, camera = "DJI_M3T")
thermaluav_correct <- tuav_correct(thermaluav, T_air = 16.1, rel_hum = 98, T_bg = NA, emiss = 1, SKC = FALSE)
tuav_export(thermaluav_correct)
```

To account for the effect of illumination changes during the flight, we applied the function *tuav_smooth()* using the method "*image*" (Section 3.2.5). The "*smooth_length*" parameter was set to the number of images in one flight line, excluding the turns. The smoothed images were also exported.

```
thermaluav_smooth <- tuav_smooth(thermaluav_correct, method = "image", smooth_length = 16)
tuav_export(thermaluav_smooth)
```

The exported images, containing the smoothed and non-smoothed brightness temperatures, were aligned and mosaicked in Agisoft Metashape Professional 2.0.0. The orthomosaic of the non-smoothed brightness, clearly shows the large change in illumination, leading to a substantial impact on the temperature data (Figure 6B). Conversely, the smoothed dataset produced a much more homogenous orthomosaic, effectively accounting for the change in illumination (Figure 6C).

5.3. Spatial emissivity correction using NDVI

With the smoothed brightness temperature orthomosaic and the corresponding NDVI map, we performed spatial emissivity correction to obtain the LST. Similar to Section 4.3, we used the *tuav_emis()* function, but now with the method *NDVI* (Section 3.2.4). This method relies on four thresholds (Section 2.2). The NDVI values for soil ($NDVI_{soil}$) and vegetation ($NDVI_{veg}$) were estimated using our NDVI map, set at 0.3 and 0.88, respectively. Emissivity values for soil ($emiss_{soil}$) and vegetation ($emiss_{veg}$) were set at 0.935 and 0.988, respectively (Heinemann et al., 2020).

```
NDVI <- terra::rast("H:/Thermal_Project/Data/M3T/250913_NDVI.tif")
T_bright_smooth <- terra::rast("H:/Thermal_Project/Data/M3T/TBright_smooth_orthomosaic.tif")
Thermaluav_emis <- tuav_emis(thermal_orig = T_bright_smooth,
                             thermal_uav = thermaluav_smooth,
                             temp = "C",
                             corrmap = NDVI,
                             method = "NDVI",
                             write_Ts = TRUE,
                             filename_Ts = "Potato_LST_smooth.tif",
                             write_emiss = TRUE,
                             NDVI_veg = 0.88,
                             NDVI_soil = 0.3,
                             emiss_veg = 0.988,
                             emiss_soil = 0.935,
                             filename_emiss = "Potato_emis.tif")
```

Using the NDVI threshold method provides more nuances in emissivity values (Figure 6E). As both brightness temperature (T_{bright}) and background temperature (T_{bg}) are close to the free air temperature, the effect of emissivity is smaller compared to Case 1 (Section 4). The final LST reaches slightly higher values compared to T_{bright} where the at-sensor temperature ($T_{at\text{-}sensor}$) is higher compared to T_{bg} (287.80 K; 14.65 °C). This is especially the case where emissivity is lower (e.g., the bare soil paths between the vegetation; Figure 6F). On locations where $T_{at\text{-}sensor}$ is lower than T_{bg}, the final LST is lower compared to T_{bright}. To provide more insight, the above-mentioned relations are plotted in Figure 7.

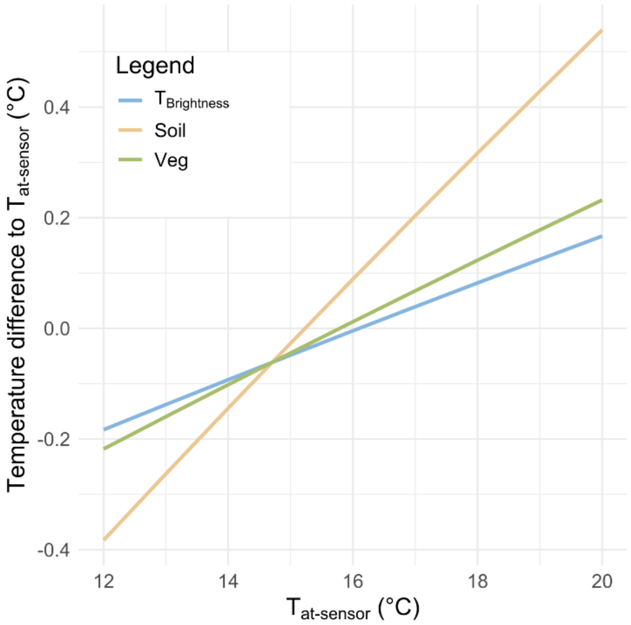

Figure 7. Temperature differences to the at-sensor temperature ($T_{at\text{-}sensor}$) in overcast conditions for Case 2. With the brightness temperature (ϵ = 1) in blue becoming higher compared to $T_{at\text{-}sensor}$ when $T_{at\text{-}sensor}$ exceeds the free air temperature. The differences to the final LST are given for soil (ϵ_{soil} = 0.935) and vegetation (ϵ_{veg} = 0.988). The differences are calculated using Eq. (6) with the mean atmospheric values during the flight: a transmittance of 0.9581, air temperature of 16.1 °C and a background temperature (T_{bg}) of 287.80 K. When $T_{at\text{-}sensor}$ exceeds T_{bg} the LST becomes higher compared to the brightness temperature due to emissivity values lower than 1. The difference becomes higher with a lower emissivity value.

6. Conclusion

The theRmalUAV R-package integrates the latest correction methods discussed in the literature into a flexible and user-friendly open-source tool. This package aims to facilitate the necessary corrections required to obtain LST from thermal UAV cameras. The thermal remote sensing background section clarifies the physics underlying the package, highlighting the importance of these corrections and addressing the knowledge gap in the use and processing of thermal UAV imagery.

The package offers two distinct workflows: an image-based workflow and an orthomosaic-based workflow. The orthomosaic workflow applies the necessary corrections at the orthomosaic level using a single function, while the image-based workflow provides additional functionalities. These include accounting for intra-flight variations in atmospheric conditions and thus atmospheric corrections (e.g., transmittance), as well as the effect of air temperature on surface temperature. Additionally, a novel method for addressing rapid changes in illumination, using temperature data from the images themselves, results in more homogeneous orthomosaics with fewer artifacts.

Other functionalities of the package encompass data cleaning, co-registration, and reporting. Furthermore, the importance of the spatial emissivity correction is emphasized, with both the NDVI method and a land cover method incorporated into both workflows. The functionalities are demonstrated through two use cases, with further details available in the package's help function and vignettes. The theRmalUAV R-package performs complete image processing while retaining the necessary metadata for alignment and mosaicking in photogrammetry software.

Declaration of Competing Interest

None.

Funding

This study was funded by Internal Funds of KU Leuven (MICROMICS project; C14/22/067).

Declaration of generative AI and AI-assisted technologies in the writing process.

During the preparation of this work the lead author used Microsoft Copilot in order to improve the readability and language of the manuscript. After using this tool, the author reviewed and edited the content as needed and takes full responsibility for the content of the published article.

Acknowledgements

The author would like to thank Wouter H. Maes for the valuable insights in thermal UAV remote sensing and the first idea of the script, Koenraad Van Meerbeek for the constructive feedback regarding the storyline and Sam Ottoy for support regarding UAV field campaigns.

References

Agisoft Metashape, 2024. MicaSense Altum processing workflow (including Reflectance Calibration) in Agisoft Metashape Professional [WWW Document]. URL https://agisoft.freshdesk.com/support/solutions/articles/31000148381-micasense-altum-processing-workflow-including-reflectance-calibration-in-agisoft-metashape-professi

Aicardi, I., Chiabrando, F., Lingua, A.M., Noardo, F., Piras, M., Vigna, B., 2017. A methodology for acquisition and processing of thermal data acquired by UAVs: a test about subfluvial springs' investigations. Geomatics, Natural Hazards and Risk 8, 5–17. https://doi.org/10.1080/19475705.2016.1225229

Allison, R.S., Johnston, J.M., Craig, G., Jennings, S., 2016. Airborne optical and thermal remote sensing for wildfire detection and monitoring. Sensors (Switzerland) 16. https://doi.org/10.3390/s16081310

Beaver, J.T., Baldwin, R.W., Messinger, M., Newbolt, C.H., Ditchkoff, S.S., Silman, M.R., 2020. Evaluating the Use of Drones Equipped with Thermal Sensors as an Effective Method for Estimating Wildlife. Wildl Soc Bull 44, 434–443. https://doi.org/10.1002/wsb.1090

Budzier, H., Gerlach, G., 2015. Calibration of uncooled thermal infrared cameras. Journal of Sensors and Sensor Systems 4, 187–197. https://doi.org/10.5194/jsss-4-187-2015

Carlson, T.N., Ripley, D.A., 1997. On the relation between NDVI, fractional vegetation cover, and leaf area index. Remote Sens Environ 62, 241–252. https://doi.org/10.1016/S0034-4257(97)00104-1

Cheng, K.H., Jiao, J.J., Luo, X., Yu, S., 2022. Effective coastal Escherichia coli monitoring by unmanned aerial vehicles (UAV) thermal infrared images. Water Res 222, 118900. https://doi.org/10.1016/j.watres.2022.118900

Cuenca, J., Sobrino, J., 2004. Experimental measurements for studying angular and spectral variation of thermal infrared emissivity. Appl Opt 43, 4598–4602. https://doi.org/10.1364/AO.43.004598

Dai, G., Wang, C., Tang, Q., He, L., Chen, H., Sunil, C.K., Dewi, C., 2025. Aerial infrared thermal imaging transmission line defect detection methods incorporating explicit visual center structures. Measurement (Lond) 245, 116605. https://doi.org/10.1016/j.measurement.2024.116605

Frolec, J., Králík, T., Musilová, V., Hanzelka, P., Srnka, A., Jelínek, J., 2019. A database of metallic materials emissivities and absorptivities for cryogenics. Cryogenics (Guildf) 97, 85–99. https://doi.org/10.1016/j.cryogenics.2018.12.003

Heinemann, S., Siegmann, B., Thonfeld, F., Muro, J., Jedmowski, C., Kemna, A., Kraska, T., Muller, O., Schultz, J., Udelhoven, T., Wilke, N., Rascher, U., 2020. Land surface temperature retrieval for agricultural areas using a novel UAV platform equipped with a thermal infrared and multispectral sensor. Remote Sens (Basel) 12. https://doi.org/10.3390/rs12071075

Henn, K.A., Peduzzi, A., 2024. Surface Heat Monitoring with High-Resolution UAV Thermal Imaging: Assessing Accuracy and Applications in Urban Environments. Remote Sens (Basel) 16. https://doi.org/10.3390/rs16050930

Hoffmann, H., Nieto, H., Jensen, R., Guzinski, R., Zarco-Tejada, P., Friborg, T., 2016. Estimating evaporation with thermal UAV data and two-source energy balance models. Hydrol Earth Syst Sci 20, 697–713. https://doi.org/10.5194/hess-20-697-2016

Hoffrén, R., García, M.B., 2023. Thermal unmanned aerial vehicles for the identification of microclimatic refugia in topographically complex areas. Remote Sens Environ 286. https://doi.org/10.1016/j.rse.2022.113427

Jones, H., Vaughan, R., 2010. Remote sensing of vegetation principles techniques and applications. Oxford university press.

Jones, H.G., Archer, N., Rotenberg, E., Casa, R., 2003. Radiation measurement for plant ecophysiology. J Exp Bot 54, 879–889. https://doi.org/10.1093/jxb/erg116

Kelly, J., Kljun, N., Olsson, P.-O., Mihai, L., Liljeblad, B., Weslien, P., Klemedtsson, L., Eklundh, L., 2019. Challenges and Best Practices for Deriving Temperature Data from an Uncalibrated UAV Thermal Infrared Camera. Remote Sens (Basel) 11. https://doi.org/10.3390/rs11050567

Kerr, Y.H., Lagouarde, J.P., Nerry, F., Ottlé, C., 2004. Land surface temperature retrieval techniques and applications, in: Quattrochi, D.A., Luvall, J.C. (Eds.), Thermal Remote Sensing in Land Surface Processing. CRC Press, p. 464. https://doi.org/https://doi.org/10.1201/9780203502174

Li, Z.L., Becker, F., 1993. Feasibility of land surface temperature and emissivity determination from AVHRR data. Remote Sens Environ 43, 67–85. https://doi.org/10.1016/0034-4257(93)90065-6

Li, Z.L., Wu, H., Wang, N., Qiu, S., Sobrino, J.A., Wan, Z., Tang, B.H., Yan, G., 2013. Land surface emissivity retrieval from satellite data. Int J Remote Sens 34, 3084–3127. https://doi.org/10.1080/01431161.2012.716540

Liao, K.C., Lu, J.H., 2021. Using uav to detect solar module fault conditions of a solar power farm with ir and visual image analysis. Applied Sciences (Switzerland) 11, 1–21. https://doi.org/10.3390/app11041835

Lillesand, T.M., Kiefer, R.W., Chipman, J.W., 2015. Remote sensing and image interpretation, 7th ed. ed. Wiley, Hoboken, NJ.

Maes, W.H., 2025. Practical Guidelines for Performing UAV Mapping Flights with Snapshot Sensors. Remote Sens (Basel) 17. https://doi.org/10.3390/rs17040606

Maes, W.H., Huete, A.R., Steppe, K., 2017. Optimizing the processing of UAV-based thermal imagery. Remote Sens (Basel) 9. https://doi.org/10.3390/rs9050476

Maes, W.H., Steppe, K., 2012. Estimating evapotranspiration and drought stress with ground-based thermal remote sensing in agriculture: a review. J Exp Bot 63, 4671–4712. https://doi.org/10.1093/jxb/ers165

Manfreda, S., McCabe, M.F., Miller, P.E., Lucas, R., Madrigal, V.P., Mallinis, G., Dor, E. Ben, Helman, D., Estes, L., Ciraolo, G., Müllerová, J., Tauro, F., de Lima, M.I., de Lima, J.L.M.P., Maltese, A., Frances, F., Caylor, K., Kohv, M., Perks, M., Ruiz-Pérez, G., Su, Z., Vico, G., Toth, B., 2018. On the use of unmanned aerial systems for environmental monitoring. Remote Sens (Basel) 10. https://doi.org/10.3390/rs10040641

Messina, G., Modica, G., 2020. Applications of UAV thermal imagery in precision agriculture: State of the art and future research outlook. Remote Sens (Basel). https://doi.org/10.3390/RS12091491

Minkina, W., Klecha, D., 2015. Modeling of Atmospheric Transmission Coefficient in Infrared for Thermovision Measurements 903–907. https://doi.org/10.5162/irs2015/1.4

Mirka, B., Stow, D.A., Paulus, G., Loerch, A.C., Coulter, L.L., An, L., Lewison, R.L., Pflüger, L.S., 2022. Evaluation of thermal infrared imaging from uninhabited aerial vehicles for arboreal wildlife surveillance. Environ Monit Assess 194, 1–15. https://doi.org/10.1007/s10661-022-10152-2

Muro, J., Strauch, A., Heinemann, S., Steinbach, S., Thonfeld, F., Waske, B., Diekkrüger, B., 2018. Land surface temperature trends as indicator of land use changes in wetlands. International Journal of Applied Earth Observation and Geoinformation 70, 62–71. https://doi.org/10.1016/j.jag.2018.02.002

Posch, C., Matolin, D., Wohlgenannt, R., Maier, T., Litzenberger, M., 2009. A microbolometer asynchronous dynamic vision sensor for LWIR. IEEE Sens J 9, 654–664. https://doi.org/10.1109/JSEN.2009.2020658

Rakha, T., Liberty, A., Gorodetsky, A., Kakillioglu, B., Velipasalar, S., 2018. Heat Mapping Drones: An Autonomous Computer-Vision-Based Procedure for Building Envelope Inspection Using Unmanned Aerial Systems (UAS). Technology Architecture and Design 2, 30–44. https://doi.org/10.1080/24751448.2018.1420963

Rubio, E., Caselles, V., Badenas, C., 1997. Emissivity measurements of several soils and vegetation types in the 8-14 µm wave band: Analysis of two field methods. Remote Sens Environ 59, 490–521. https://doi.org/10.1016/S0034-4257(96)00123-X

Rudol, P., Doherty, P., 2008. Human body detection and geolocalization for UAV search and rescue missions using color and thermal imagery. IEEE Aerospace Conference Proceedings. https://doi.org/10.1109/AERO.2008.4526559

Salisbury, John W., D’Aria, D.M., 1992. Emissivity of terrestrial materials in the 8–14 µm atmospheric window. Remote Sens Environ 42, 83–106. https://doi.org/10.1016/0034-4257(92)90092-X

Santesteban, L.G., Di Gennaro, S.F., Herrero-Langreo, A., Miranda, C., Royo, J.B., Matese, A., 2017. High-resolution UAV-based thermal imaging to estimate the instantaneous and seasonal variability of plant water status within a vineyard. Agric Water Manag 183, 49–59. https://doi.org/10.1016/j.agwat.2016.08.026

Sedlar, J., Hock, R., 2009. Testing longwave radiation parameterizations under clear and overcast skies at Storglaciären, Sweden. Cryosphere 3, 75–84. https://doi.org/10.5194/tc-3-75-2009

Sobrino, J.A., El Kharraz, J.., Li, Z.L., 2003. Surface temperature and water vapour retrieval from MODIS data. Int J Remote Sens 24, 5161–5182. https://doi.org/10.1080/0143116031000102502

Sobrino, J.A., Jiménez-Muñoz, J.C., Sòria, G., Romaguera, M., Guanter, L., Moreno, J., Plaza, A., Martínez, P., 2008. Land surface emissivity retrieval from different VNIR and TIR sensors. IEEE Transactions on Geoscience and Remote Sensing 46, 316–327. https://doi.org/10.1109/TGRS.2007.904834

Sobrino, J.A., Raissouni, N., 2000. Toward remote sensing methods for land cover dynamic monitoring: Application to Morocco. Int J Remote Sens 21, 353–366. https://doi.org/10.1080/014311600210876

Stutsel, B., Johansen, K., Malbéteau, Y.M., McCabe, M.F., 2021. Detecting Plant Stress Using Thermal and Optical Imagery From an Unoccupied Aerial Vehicle. Front Plant Sci 12. https://doi.org/10.3389/fpls.2021.734944

Tang, B.H., Shao, K., Li, Z.L., Wu, H., Tang, R., 2015. An improved NDVI-based threshold method for estimating land surface emissivity using MODIS satellite data. Int J Remote Sens 36, 4864–4878. https://doi.org/10.1080/01431161.2015.1040132

Tran, Q.H., Han, D., Kang, C., Haldar, A., Huh, J., 2017. Effects of ambient temperature and relative humidity on subsurface defect detection in concrete structures by active thermal imaging. Sensors (Switzerland) 17, 1–18. https://doi.org/10.3390/s17081718

Valor, E., Caselles, V., 1996. Mapping land surface emissivity from NDVI: Application to European, African, and South American areas. Remote Sens Environ 57, 167–184. https://doi.org/10.1016/0034-4257(96)00039-9

Van de Griend, A.A., Owe, M., 1993. On the relationship between thermal emissivity and the normalized difference vegetation index for natural surfaces. Int J Remote Sens 14, 1119–1131. https://doi.org/10.1080/01431169308904400

Vlaminck, M., Heidbuchel, R., Philips, W., Luong, H., 2022. Region-Based CNN for Anomaly Detection in PV Power Plants Using Aerial Imagery. Sensors 22, 1–18. https://doi.org/10.3390/s22031244

Wang, Y., Yang, Z., Khan, H.A., Kootstra, G., 2024. Improving Radiometric Block Adjustment for UAV Multispectral Imagery under Variable Illumination Conditions. Remote Sens (Basel) 16, 1–27. https://doi.org/10.3390/rs16163019

Wood, R.A., Han, C.J., Kruse, P.W., 1992. Integrated uncooled infrared detector imaging arrays, in: Technical Digest IEEE Solid-State Sensor and Actuator Workshop. pp. 132–135. https://doi.org/10.1109/SOLSEN.1992.228308

Wu, Y., Shan, Y., Lai, Y., Zhou, S., 2022. Method of calculating land surface temperatures based on the low-altitude UAV thermal infrared remote sensing data and the near-ground meteorological data. Sustain Cities Soc 78, 103615. https://doi.org/10.1016/j.scs.2021.103615

754